

1 Southern Ocean Overturning Compensation in an Eddy-Resolving Climate

2 Simulation

Stuart P. Bishop*

North Carolina State University, Raleigh, North Carolina

Peter R. Gent, Frank O. Bryan

National Center for Atmospheric Research, Boulder, Colorado

Andrew F. Thompson

California Institute of Technology, Pasadena, California

Matthew C. Long

National Center for Atmospheric Research, Boulder, Colorado

Ryan Abernathy

Columbia University, New York, New York

¹³ *Corresponding author address: Department of Marine, Earth, and Atmospheric Sciences, North
Carolina State University, Campus Box 8208, Raleigh, NC 27695
¹⁴
¹⁵ E-mail: spbishop@ncsu.edu

ABSTRACT

The Southern Ocean's Antarctic Circumpolar Current (ACC) and Meridional Overturning Circulation (MOC) response to increasing zonal wind stress is for the first time analyzed in a high-resolution (0.1° ocean and 0.25° atmosphere) fully-coupled global climate simulation using the Community Earth System Model. Results from a 20-year wind perturbation experiment, where the Southern Hemisphere zonal wind stress is increased by 50% south of 30°S , show only marginal changes in the mean ACC transport through Drake Passage; an increase of 6% (136 to 144 Sv) in the perturbation experiment compared with the control. However, the upper and lower circulation cells of the MOC do change. The lower cell is more affected than the upper cell with a maximum increase of 64% versus 39% respectively. Changes in the MOC are directly linked to changes in water mass transformation from shifting surface isopycnals and sea ice melt, giving rise to changes in surface buoyancy forcing. The increase in transport of the lower cell leads to upwelling of warm and salty Circumpolar Deep Water and subsequent melting of sea ice surrounding Antarctica. The MOC is commonly supposed to be the sum of two opposing components: a wind- and transient-eddy overturning cell. Here, the transient-eddy overturning is virtually unchanged due to a large-scale cancellation of localized regions of both enhancement and suppression of eddy kinetic energy along the mean path of the ACC. However, decomposing the steady overturning into a time and zonal mean component and a standing-eddy component, reveals partial compensation between wind-driven and standing-eddy components of the circulation.

³⁹ **1. Introduction**

⁴⁰ It is currently estimated that greater than 40% of the oceanic uptake of anthropogenic CO₂ takes
⁴¹ place south of 40°S (Sallée et al. 2012) and mesoscale eddies play an important role in the uptake
⁴² (Gnanadesikan et al. 2015). The oceanic uptake over the Southern Ocean is largely governed by
⁴³ the strength of the meridional overturning circulation (MOC) and where wind-induced upwelling
⁴⁴ of isopycnal surfaces outcrop (Marshall and Speer 2012; Morrison et al. 2015). Over the past fifty
⁴⁵ years, Southern Ocean winds have been increasing at a steady rate and have shifted poleward in
⁴⁶ response to anthropogenic forcing from the Antarctic ozone hole in the lower stratosphere and
⁴⁷ global climate change (Thompson et al. 2011). Recent work from paleo records suggests that the
⁴⁸ Southern Ocean winds have been weaker in past climates due to an equatorward shift of the polar
⁴⁹ Westerlies (Toggweiler 2009) and are currently the strongest they have been in the past thousand
⁵⁰ years (Abram et al. 2014). Understanding how the strength of the Antarctic Circumpolar Current
⁵¹ (ACC) and MOC response to changing winds is fundamental to understanding global climate
⁵² change.

⁵³ The ACC and MOC response to changing surface wind and buoyancy forcing hinges on the
⁵⁴ response by mesoscale eddies. One hypothesis is that there will be zero change in ACC trans-
⁵⁵ port with increasing winds. The paradigm is that as winds increase, the ACC transport will not,
⁵⁶ because wind-forced steepening of isopycnals will quickly be brought back to their original state
⁵⁷ through eddy-induced advection. Down-gradient eddy buoyancy fluxes generated via baroclinic
⁵⁸ instability draw on the excess available potential energy imparted by the increase in zonal wind
⁵⁹ stress. The near independence of the ACC transport (usually through Drake Passage) to changes
⁶⁰ in the Southern Hemisphere wind stress is commonly referred to as *eddy saturation* (Straub 1993;
⁶¹ Munday et al. 2013). Near eddy saturation is becoming more widely accepted as limited observa-

62 tions (Firing et al. 2011; Chidichimo et al. 2014; Böning et al. 2008) and modeling efforts (Farneti
63 et al. 2015) see only small trends in ACC transport over the period of increased wind forcing.

64 It is less clear how the Southern Ocean’s zonally-integrated secondary circulation responds to
65 changing winds. Theories suggest that the Southern Ocean MOC is the small residual of the
66 near cancelation of two opposing meridional circulation cells; a clockwise (looking west) wind-
67 driven circulation in the density-latitude plane (equatorward at the surface and poleward at depth)
68 known as the “Deacon Cell” and an eddy-driven cell of opposite sense (Johnson and Bryden 1989;
69 Marshall and Radko 2003). The near independence of the MOC to changes in winds is referred to
70 as *eddy compensation* because any changes to the wind-driven Deacon Cell will be compensated
71 by the eddy-driven circulation. Any changes in the MOC too must be consistent with surface
72 buoyancy flux changes indirectly related to changes in the wind field, which results in water mass
73 transformation.

74 The degree of eddy compensation presently taking place in the Southern Ocean is still unknown,
75 but there is observational evidence from satellite altimetry that eddy kinetic energy (EKE) has in-
76 creased in recent decades (Meredith and Hogg 2006; Hogg et al. 2015). A general lack of oceanic
77 observations have made direct diagnosis of the MOC unattainable so that there is no “true” esti-
78 mate for models to use as a benchmark. Estimates of the MOC from models that most realistically
79 represent the ocean are instead used as a “true” depiction of the MOC. Recent work by Farneti
80 et al. (2015) shows that there is considerable spread in the strength of the MOC across coarse-
81 resolution (1°) models forced with CORE-II winds (Large and Yeager 2009) and amongst coupled
82 climate models (Downes and Hogg 2013). Climate models rely on an accurate representation
83 of mesoscale eddies, which are not routinely resolved in climate models and are parameterized
84 (Gent and McWilliams 1990) (hereafter referred to as GM). Idealized studies show that the MOC

85 response is more sensitive to model resolution than is the ACC transport (Stewart et al. 2014;
86 Morrison and Hogg 2013).

87 To address how the MOC will respond to changing winds, a wide range of model experiments
88 have been performed from idealized zonally-re-entrant channels to more realistic global circulation
89 models. For an extensive review of the effects of Southern Hemisphere wind changes on the MOC
90 in ocean models see Gent (2015). Idealized studies that are eddy resolving show that there is partial
91 eddy compensation, but results depend on surface boundary conditions (Abernathy et al. 2011;
92 Wolfe and Cessi 2010). Gent and Danabasoglu (2011) (hereafter referred to as GD11) show that
93 in a realistic coupled climate model, eddy compensation is achieved if the GM eddy coefficient is
94 allowed to vary in space and time in response to changes in stratification, which is consistent with
95 idealized studies where EKE increases with winds (Abernathy et al. 2011; Morrison and Hogg
96 2013). The highest resolution global simulation to date to investigate MOC changes due to wind
97 forcing is in an eddy-permitting model ($1/6^\circ$) that is uncoupled to the atmosphere (Hallberg and
98 Gnanadesikan 2006). However, this model's representation of Southern Ocean mesoscale eddies
99 might be under-resolved, because the first baroclinic deformation radius, which is the characteristic
100 spatial length scale of mesoscale eddies and ranges from 6–25 km in the Southern Ocean (Smith
101 2007), requires higher than $1/6^\circ$ resolution south of 30°S (Hallberg 2013).

102 To overcome uncertainty regarding the parameterization and resolution of mesoscale eddies,
103 this study examines the ACC transport and MOC response to changing winds in a new, high-
104 resolution version of the Community Earth System Model (CESM). The experiment is conducted
105 with a fully coupled configuration of CESM with an eddy resolving (0.1°) ocean component and
106 high-resolution (0.25°) atmosphere. The increase in resolution compared to a standard CESM
107 simulation at coarse resolution (1° ocean and atmosphere) can be seen from snap shots of sea
108 surface temperature (SST) and sea surface height (SSH) in Fig. 1. When mesoscale eddies are

109 explicitly resolved there is more filamentary structure and closed contours of SSH. With this high-
110 resolution version of CESM we test the ideas of eddy saturation and eddy compensation by running
111 a twenty-year wind perturbation (WP) experiment in which the zonal wind stress in the Southern
112 Ocean south of 30°S is increased by 50%, the same as the PERT1 experiment in GD11. This is
113 the highest resolution simulation brought to bear on this problem to date.

114 One of the interesting results of this study is that standing eddies play the dominant role in the
115 response of the MOC to increasing winds compared to transient eddies. Standing eddies were
116 recognized as a major contributor to meridional fluxes in the Southern Ocean by early studies
117 (de Szoeke and Levine 1981; Treguier and McWilliams 1990; Wolff et al. 1991). However, popular
118 theoretical models of the ACC are framed in terms of a “streamwise average,” which follows the
119 meanders of the time-mean current, effectively eliminating the standing component and leaving
120 a balance between a wind-driven Ekman component and a transient eddy component (Marshall
121 et al. 1993; Marshall and Radko 2003; Nikurashin and Vallis 2012). Recent studies have re-
122 emphasized the importance of standing eddies for the time-mean meridional flux of heat in the
123 Southern Ocean (Volkov et al. 2010) and in the response to wind perturbations (Thompson and
124 Garabato 2014; Abernathey and Cessi 2014; Dufour et al. 2012; Viebahn and Eden 2012; Zika
125 et al. 2013). In our WP experiment the eddy kinetic energy (EKE) doesn’t increase uniformly
126 (Fig. 2), but is both actually enhanced and suppressed along the mean path of the ACC without a
127 systematic shift of the ocean fronts. Due to this EKE response, there is very little change in the
128 zonally-integrated transient eddy overturning. Instead, the standing eddy component responds to
129 partially compensate for changes in the wind-driven circulation.

130 The paper is organized as follows. In the next section the MOC and its constituents are defined.
131 In section 3 the control and WP experiments using high-resolution CESM are described. Section
132 4 shows the results of the ACC transport and MOC response in the WP experiment compared to

133 the control simulation. Section 5 discusses the importance of the standing component of the mean
 134 overturning circulation in the MOC balance. Section 6 makes the connection between water mass
 135 modification and changes in the MOC. Lastly, section 7 contains a discussion and the conclusions
 136 of our results.

137 **2. Meridional Overturning Circulation**

138 The Southern Ocean MOC in depth space, referred to here as the Eulerian-mean MOC, is cal-
 139 culated by integrating the meridional velocity, v , zonally and vertically,

$$\psi(y, z) = \overline{\oint \int_z^0 v dz' dx}, \quad (1)$$

140 where x and z are the zonal and vertical coordinates respectively. The overbar indicates a time
 141 average, $\overline{(\)} \equiv \frac{1}{\tau} \int_0^\tau (\) dt$, where τ is the averaging period. This representation of the MOC is
 142 largely made up of the wind-driven Ekman circulation which is well known as the “Deacon Cell.”
 143 It was later realized by Döös and Webb (1994) that the Deacon Cell vanishes when the MOC is
 144 calculated vertically in density rather than depth space. The overturning circulation calculated in
 145 density space better represents water mass transport, which is largely along isopycnals in the ACC
 146 and consistent with the net overturning resulting from two opposing mechanisms; the wind-driven
 147 circulation of the Deacon Cell and the eddy- driven circulation. The MOC is defined as

$$\psi_{moc}(y, \sigma) = \overline{\oint \int_\sigma^{\sigma_s} v h d\sigma' dx}, \quad (2)$$

148 where $h(x, y, \sigma, t) \equiv -\partial \tilde{z}/\partial \sigma$ is the thickness of isopycnal layers, \tilde{z} is the depth of isopycnal
 149 surfaces, and σ_s is the surface isopycnal surface. σ is potential density and in practice σ_2 (potential
 150 density referenced to 2000 m depth) is used to calculate the MOC since its vertical structure tends
 151 to have monotonic profiles and is a good representation of the MOC calculated in neutral density
 152 classes (Lee and Coward 2003). As mentioned above ψ_{moc} can be thought of as consisting of two

₁₅₃ opposing cells between the wind-driven overturning circulation, $\bar{\psi}$, and transient eddy-induced
₁₅₄ overturning circulation, ψ^* ,

$$\psi_{\text{moc}}(y, \sigma) = \bar{\psi} + \psi^*. \quad (3)$$

₁₅₅ The steady overturning circulation in isopycnal coordinates is defined as

$$\bar{\psi}(y, \sigma) = \oint \int_{\bar{\sigma}}^{\bar{\sigma}_s} \bar{v} \bar{h} d\sigma' dx, \quad (4)$$

₁₅₆ where $\bar{h}(x, y, \sigma)$ is the time mean thickness of isopycnal layers. The transient-eddy-induced over-
₁₅₇ turning circulation is given by the difference between the residual and steady streamfunctions as

$$\psi^*(y, \sigma) = \psi_{\text{moc}} - \bar{\psi} = \overline{\oint \int_{\sigma}^{\bar{\sigma}_s} v' h' d\sigma' dx}, \quad (5)$$

₁₅₈ where the prime indicates a deviation from the time mean.

₁₅₉ 3. Model

₁₆₀ a. Control experiment

₁₆₁ The model used in this study is a high-resolution version of the CESM (Hurrell et al. 2013),
₁₆₂ a new generation climate system model that is the successor to the Community Climate System
₁₆₃ Model version 4 (Gent et al. 2011). Details of the simulation examined are summarized below,
₁₆₄ but for a more in depth description see Small et al. (2014). The model configuration includes
₁₆₅ the Community Atmosphere Model version 5 (CAM5) with a spectral element dynamical core,
₁₆₆ Community Ice Code version 4 (Hunke and Lipscomb 2008), Parallel Ocean Program version 2
₁₆₇ (POP2), and Community Land Model version 4 (Lawrence et al. 2011). CAM5 was integrated
₁₆₈ with a horizontal resolution of about 0.25 degrees (specifically the spectral element dynamical
₁₆₉ core with 120 elements on each face of the cubed sphere, referred to as ne120) and 30 levels in the
₁₇₀ vertical.

171 The POP2 model has a nominal grid spacing of 0.1 degrees (decreasing from 11 km at the
172 Equator to 2.5 km at high latitudes) on a tripole grid with poles in North America and Asia. The
173 configuration is similar to that used in McClean et al. (2011) and Kirtman et al. (2012), except
174 that the number of vertical levels was increased from 42 to 62, with more levels in the main ther-
175 mocline. The ocean communicated with the coupler, providing updated SST and surface currents
176 and receiving updated surface fluxes, every 6 hours and the atmosphere communicated every 10
177 minutes. The coupler computes air-sea fluxes using the Large and Yeager (2009) surface layer
178 scheme. The land and sea ice models are on the same grids as the atmosphere and ocean mod-
179 els respectively. POP2 has been shown to produce eddy covariances consistent with observations
180 in the Pacific (Bishop and Bryan 2013) and Southern Ocean (Lenn et al. 2011), and this high-
181 resolution version of CESM through spectral analysis produces mesoscale eddy covariances of
182 SST and geostrophic meridional velocity which are consistent with satellite observations (Aber-
183 nathey and Wortham 2015). The simulation was run for 86 years following a 15 year spin up for
184 a total of 101 years and the ocean was initialized with WOCE climatology derived from Gouret-
185 ski and Koltermann (2004). The CESM was run under “present-day (year 2000)” greenhouse gas
186 conditions (fixed CO₂ concentration of 367 ppm). The model years in this analysis will refer to
187 the last 86 years of the simulation with model year 1 being equivalent to aggregate simulation year
188 16. Time averages and covariances of three-dimensional variables for the atmosphere and ocean
189 were archived monthly. For the current work we will focus on model years 45–66, which are the
190 model years when the WP experiment was performed.

191 *b. Wind Perturbation Experiment*

192 In this section we describe the WP experiment where the Southern Hemisphere zonal wind
193 stress is increased by 50%. The WP experiment was conducted with the same methodology as

194 the PERT1 experiment in GD11, but here using CESM rather than CCSM4. The WP experiment
195 is a 22-year simulation starting from year 45 of the control simulation. The WP experiment was
196 conducted by multiplying the zonal wind stress forcing the ocean component by 1.5 south of 35°S,
197 with this factor linearly reducing to 1 between 35° and 25°S. The maximum time and zonal mean
198 Southern Hemisphere wind stress is 41% larger compared with the control for model years 56–66
199 with an increase of 0.083 N m^{-2} from 0.197 N m^{-2} in the control to 0.280 N m^{-2} in WP (Fig.
200 3a), which is very close to the maximum wind stress values cited in GD11.

201 The increased zonal wind stress was not used in the bulk formulae to calculate the atmosphere-
202 to-ocean heat and freshwater fluxes, and the increased zonal stress is not felt directly by the atmo-
203 sphere component. There is an indirect effect on the coupled system, however, through changes to
204 the SST, and this is reflected in changes to net surface buoyancy flux (\mathcal{B}). Mean changes in den-
205 sity, SST, and sea-surface salinity (SSS) are shown in Fig. 4. Surface density is increased almost
206 uniformly along the ACC, and the patches of less dense waters are north of 45°S (Fig. 4a). The
207 zonal average shows that the surface waters are more dense at all latitudes except near 30°S and
208 the increase peaks near 50°S (Fig. 4b). The changes in SST and SSS reflect this increase in den-
209 sity. Water spanning 10–20° latitude surrounding Antarctica are warmer and saltier by as much
210 as 1–2°C and $0.25\text{--}0.5 \text{ g kg}^{-1}$ respectively (Fig.s 4c,e). The warmer and saltier waters around
211 Antarctica are mostly density compensated with small changes in density, but an overall increase.
212 Water is much cooler in patches along the ACC and throughout most of the Pacific and Indian
213 oceans, but salinity changes are less prevalent except water is fresher near 30°S in the Pacific. The
214 zonal average SST and SSS show that the surface waters are more salty at latitudes south of 30°
215 (Fig. 4f), but zonal average SST is only warmer south of 50°S (Fig. 4d).

216 Differences in surface buoyancy flux are closely tied to changes in the MOC. For example,
217 increased upwelling of cold water can lead to cooler SSTs and consequently a decrease in latent

and sensible heat flux. As described in the theoretical model of Marshall and Radko (2003), the net upwelling and subduction in and out of the surface layer must be balanced by diabatic processes (air-sea fluxes and mixing) within the surface layer. In an idealized, ocean-only, eddy-resolving model, Abernathey et al. (2011) showed how wind perturbation experiments could lead to different MOC changes depending on the details of the surface buoyancy boundary conditions. Only a coupled climate model, such as the one examined here, can hope to represent the full range of feedbacks which govern the changes in SST, surface buoyancy flux, and MOC in response to a wind perturbation. In Sec. 6, we examine the connection between changes in surface buoyancy flux, \mathcal{B} , and changes in overturning through the lens of water mass transformation.

4. Results

a. Antarctic Circumpolar Current Transport Response

The ACC transport through Drake Passage is shown in Fig. 3b. The mean and standard deviation for the control and WP are 136 ± 3 Sv and 144 ± 6 Sv, respectively. The WP time series has a trend over the first ten years of 23 Sv decade $^{-1}$ with a small negative trend over the last ten years of -6 Sv decade $^{-1}$. The overall WP mean transport only increases by 6% with a 41% increase in the zonal wind stress compared to the control simulation. These results suggest that the ACC transport is largely *eddy saturated*. With this paradigm in mind it is likely that 85% of the increased momentum flux in WP is balanced by bottom form drag, with the momentum transport from the surface to the bottom being facilitated by interfacial form stress through an increase in stationary and transient eddy fluxes. However, this process is not confirmed in this study. Since it will be shown in Section 5 that standing eddies make a larger contribution to the meridional heat flux

239 compared with transient eddies (Volkov et al. 2010; Abernathey and Cessi 2014), it seems likely
240 that they also dominate the form stress and play a central role in eddy saturation.

241 The area-average EKE south of 30°S increased immediately following the change in wind stress
242 and then continued to increase for a period of 10 years, before stabilizing at a value 28% higher
243 than the control mean (Fig. 5a). The area-average EKE has a linear trend over the first ten years
244 of $26 \text{ cm}^2 \text{ s}^{-2} \text{ decade}^{-1}$, but no trend in the last ten years. However, the spatial distribution of
245 the EKE trends over the first ten years has positive and negative trends that are $O(\pm 100) \text{ cm}^2 \text{ s}^{-2}$
246 decade^{-1} (Fig. 5b), resembling the mean EKE difference over the last ten years of the simulation
247 (Fig. 2). This shows that there is both regions of enhancement and suppression of EKE with
248 increased zonal wind stress. Outside of the Malvinas and the Agulhas return flows, the positive
249 trends are largely in regions where standing meanders of the mean flow occur in the lee of ma-
250 jor topographic features, as shown in Thompson and Garabato (2014) and Abernathey and Cessi
251 (2014). The response in EKE during the first ten years reflects the linear trend in ACC transport
252 through Drake Passage (Fig. 3b). Once the area-average EKE reaches an asymptote of $\sim 35 \text{ cm}^2$
253 s^{-2} above the control mean, the ACC transport adjusts to the elevated EKE.

254 The small increase in ACC transport is also reflected in the differences in isopycnal surfaces
255 between simulations (Fig. 6). The increase in density is at most 0.16 kg m^{-3} . The differences are
256 largely focused in the upper ocean; in particular the top 100 meters within the mixed layer (Fig.
257 6b). There are only small changes in the interior (Fig. 6a). The top 100 meters is characterized by
258 more dense water in WP than the control (Fig. 4a,b). There is also less dense waters at depth north
259 of 45°S. This represents a surface intensified steepening of isopycnal surfaces, which makes up
260 the increase in the ACC transport. On average the water is more dense with a skewed probability
261 density distribution (Fig. 6c).

262 b. Meridional Overturning Circulation Response

263 1) EULERIAN-MEAN MERIDIONAL OVERTURNING CIRCULATION

264 The mean overturning streamfunction calculated in depth space (Eq. 1) is shown in Fig. 7. The
265 mean overturning streamfunction is made up of the clockwise (looking west) wind-driven circu-
266 lation in depth- latitude space, the Deacon Cell, and a weaker counterclockwise circulating lower
267 cell. As expected with the increased winds in the WP simulation, the Deacon Cell is intensified.
268 The peak values of the Deacon cell are 40.5 Sv and 57.1 Sv in the control and WP respectively
269 (Fig. 7 a,b). The latitude and depth of the maximum values of the Deacon Cell are not very differ-
270 ent between simulations. The latitude and depth of the maximum value of the Deacon cell in the
271 control simulation is 51.8°S and 607 m respectively (Fig. 7a). In WP they are 51.6°S and 552 m
272 respectively (Fig. 7b). The maximum increase in the Deacon Cell between the control and WP is
273 17 Sv and occurs at 48.3°S and at 830 m depth, which is exactly the 41% increase in zonal wind
274 stress over the control (Fig. 7c).

275 The lower cell is reduced slightly between the control and WP (Fig 7c). The maximum values
276 of the lower cell circulation are -14.7 Sv and -13.5 Sv in the control and WP respectively. The
277 latitude and depth of the maximum value of the lower cell in the control simulation is 36.9°S and
278 3752 m respectively (Fig 7a). In WP they are 36.6°S and 3752 m respectively (Fig. 7b).

279 2) MERIDIONAL OVERTURNING CIRCULATION

280 The MOC (Eq. 2) is shown in Fig. 8a–c. Comparing against a schematic of the overturning [Fig.
281 18 in Farneti et al. (2015)] there are four distinct circulation cells, but there are only two cells that
282 change substantially between our simulations which will be described. There is a clockwise-
283 rotating (looking west) upper cell centered at 48.1°S and $36.2\sigma_2$ with a maximum of 19.8 Sv in
284 the control (Fig. 8a). The upper cell in WP is centered at 48°S and $36.35\sigma_2$ with a maximum of

285 27.5 Sv (Fig. 8b). The upper cell increased by a maximum of 7.7 Sv, which is a 39% increase over
286 the control (Fig. 8c).

287 There is a counter-clockwise-rotating cell called the lower cell that has an enhanced poleward
288 region called the Subpolar cell. The Subpolar cell has a maximum of -20 Sv at 63.5°S and $37.15\sigma_2$
289 in the control (Fig. 8a). In WP the Subpolar cell has a maximum of -32.7 Sv at 64°S and $37.15\sigma_2$
290 (Fig. 8b). The counter circulation of the Subpolar cell increased by a maximum of 12.6 Sv in
291 WP compared with the control, which is a 64% increase over the control (Fig. 8c). The lower
292 cell equatorward of 50°S has no difference between simulations, indicating that it is compensated
293 between the simulations; (Fig. 8c).

294 One decomposition of the MOC is between the steady overturning (Eq. 4) and the transient-
295 eddy-induced overturning (Eq. 5) as stated in Equation 3. When we examine this decomposition,
296 we see that the mean overturning streamfunction (Fig. 8d–f) has a nearly identical structure of
297 circulation cells to the MOC (Fig. 8a–c). The upper cell has a clockwise circulation with a
298 maximum of 22.3 Sv at 52.2°S and $36.45\sigma_2$ in the control (Fig. 8d). In WP the mean upper cell
299 has a maximum of 30.7 Sv at 48.3°S and $36.30\sigma_2$ (Fig. 8e). The difference in the maximum values
300 of the upper cell is 8.4 Sv, which is a 38% increase over the control simulation (Fig. 8f). The lower
301 Subpolar cell has as a maximum value of -19.6 Sv at 64.5°S and $37.15\sigma_2$ in the control (Fig. 8d).
302 In WP it has a maximum value of -30.9 Sv at 65.2°S and $37.15\sigma_2$ (Fig. 8e). The Subpolar cell is
303 increased by 11.3 Sv, which is a 58% increase over the control (Fig. 8f).

304 The transient-eddy-induced streamfunction has a much different structure than the MOC or the
305 mean (Fig. 8 g–i). There are two counter circulating cells; an upper and a deep. The upper cell
306 is the stronger of the two and has a maximum of -16.7 Sv at 43.7°S and $35.30\sigma_2$ for the control
307 (Fig. 8 g). The upper cell in WP has a maximum of -20.5 Sv at 43.4°S and $35.30\sigma_2$ (Fig. 8h). The
308 small differences between the two simulations are at most ± 5 Sv concentrated in the upper cell

309 with virtually no change between the lower cells (Fig. 8i). Overall, the transient eddy component
 310 does not make a large contribution to the zonal-mean overturning, as seen also in Dufour et al.
 311 (2012). However, an analysis in streamwise coordinates (not performed here) would likely find a
 312 much greater role for transient eddies (Viebahn and Eden 2012; Abernathey and Cessi 2014).

313 **5. Steady Meridional Overturning Streamfunction**

314 In the previous section it was shown that little or no eddy compensation is visible when the MOC
 315 is decomposed into steady and transient components. Much of the change in the MOC is reflected
 316 in the mean MOC (Fig. 8c,f). This prompted further investigation into the mean overturning
 317 streamfunction. The steady overturning circulation, $\bar{\psi}$, can be decomposed into a time and zonal
 318 mean streamfunction, $[\bar{\psi}]$, and a deviation from the zonal mean as the “standing” component ψ^\dagger ,

$$\bar{\psi} = [\bar{\psi}] + \psi^\dagger. \quad (6)$$

319 $[\bar{\psi}]$ is defined as

$$[\bar{\psi}](y, \sigma) = \oint \int_{[\sigma]}^{[\sigma_s]} [\bar{v}] [\bar{h}] d\sigma' dx \quad (7)$$

320 where $[\]$ is a zonal average, $[\] \equiv \frac{1}{L(y)} \oint (\) dx$, and $L(y)$ is the circumpolar length that is a function
 321 of latitude. The overturning streamfunction is finally written as the three-part balance

$$\psi_{moc} = [\bar{\psi}] + \psi^\dagger + \psi^*. \quad (8)$$

322 The time and zonal mean component is essentially the Eulerian-mean MOC (Fig. 7) and
 323 remapped to the time and zonal mean depth of σ_2 surfaces (Fig. 9d–f). The differences in cir-
 324 culation cells then are equivalent to the values stated for the Deacon Cell and lower cell in the
 325 subsection 4.b. This decomposition is more physically insightful, because $[\bar{\psi}]$ is directly propor-
 326 tional to the zonal mean Ekman transport and is therefore clearly wind driven.

327 The standing component of the MOC is shown in Fig. 9g–i. Similar to the transient component it
 328 has two counter cells that are comparable in strength; an upper and lower. However, the standing
 329 component is much stronger than the time and zonal mean component. The upper cell has a
 330 maximum of -39.9 Sv at 51.5°S and $35.8\sigma_2$ in the control (Fig. 9g). The upper cell in WP has a
 331 maximum of -54.7 Sv at 51.1°S and $35.9\sigma_2$ (Fig. 9h). The upper cell increased by 14.8 Sv, which
 332 is 37% over the control (Fig. 9i).

333 The lower cell of the standing component has a maximum of -39.1 Sv at 57.8°S and $37.1\sigma_2$ in
 334 the control (Fig. 9g). In WP the maximum is -61.8 Sv at 57.8°S and $37.12\sigma_2$ (Fig. 9h). There is a
 335 22.7 Sv increase in the lower cell circulation, which is a 58% increase over the control (Fig. 9i).

336 From this analysis it is clear that a large degree of compensation exists between the wind-driven
 337 time- and zonal-mean cell and the standing component of the overturning circulation, in both the
 338 control experiment and in response to the wind perturbation,

$$\delta\psi_{\text{moc}} \approx \delta[\bar{\psi}] + \delta\psi^\dagger. \quad (9)$$

339 The time-mean kinetic energy, $\bar{K} = \frac{1}{2}(\bar{u}^2 + \bar{v}^2)$, also reflects changes in the zonal distribution of ki-
 340 netic energy. The mean kinetic energy can be decomposed into a time and zonal mean component
 341 and a standing component,

$$\bar{K} = \underbrace{\frac{1}{2}([\bar{u}]^2 + [\bar{v}]^2)}_{\text{Mean}} + \underbrace{\frac{1}{2}([u^\dagger]^2 + [v^\dagger]^2)}_{\text{Standing}}. \quad (10)$$

342 The change between the WP and control simulations of the two components of Eq. 10 are shown
 343 in Fig. 10. The biggest changes in the kinetic energy are in the standing component. This suggests
 344 that longitudinal variations in the velocity field between simulations is giving rise to enhanced
 345 mean kinetic energy.

346 **6. Surface Water Mass Transformation**

347 To better understand the thermodynamics of the changes in the MOC, in this section we describe
348 an analysis of surface water mass transformation. Here “water mass transformation” refers to the
349 thermodynamic modification of water density due to diabatic processes such as surface fluxes and
350 mixing. When the transformation rates are integrated over isopycnals in an ocean basin, the net
351 transformation must balance the inflow / outflow in density coordinates, i.e. the MOC defined in
352 Eq. 2 (Walsh 1982; Tziperman 1986; Speer and Tziperman 1992; Marshall et al. 1999; Marsh
353 et al. 2000; Large and Nurser 2001; Iudicone et al. 2008; Downes et al. 2015). We can therefore
354 expect the changes in Eq. 2 under wind perturbation to be accompanied by changes in water mass
355 transformation rates.

356 Changes in the surface buoyancy flux between the simulations are shown in Fig. 11. Surface
357 buoyancy flux is the sum of surface heat flux (Q_o) and fresh-water flux (FWF),

$$\mathcal{B} = \frac{\alpha_\theta g}{\rho_o c_p} Q_o - \frac{\alpha_S g}{\rho_{fw}} S_o (E - P - R) \quad (11)$$

358 where $\alpha_\theta = \partial\sigma/\partial\theta$, σ is potential density, θ is potential temperature, $\alpha_S = \partial\sigma/\partial S$ and S is
359 salinity, $E - P - R$ is the surface FWF (evaporation minus precipitation minus runoff), g is the
360 acceleration due to gravity, $\rho_o = 1026$ is the ocean reference density, $c_p = 3996 \text{ J kg}^{-1} \text{ K}^{-1}$ is the
361 specific heat at constant pressure for seawater, $S_o = 34.7 \text{ g kg}^{-1}$ is the ocean reference salinity for
362 the virtual salt flux, and $\rho_{fw} = 1000 \text{ kg m}^{-3}$ is the density of fresh water. The change in \mathcal{B} shows
363 a complex spatial pattern with a net buoyancy flux reduction near the coast of Antarctica and to
364 the north along the southern fringes of the subtropical gyres with pockets of net buoyancy flux
365 increase and decrease along the ACC track (Fig. 11a). The sign convention of negative means the
366 ocean is losing heat. The zonally-averaged \mathcal{B} as a function of latitude takes the familiar sinusoidal
367 meridional structure (Fig. 11b). The changes in surface heat flux (Fig. 11c) dominate buoyancy

368 forcing compared with FWFs (Fig. 11e). The FWF spatial difference (Fig. 11e) and zonal average
 369 difference (Fig. 11f) both show positive buoyancy forcing near Antarctica. This is consistent with
 370 sea ice loss between the simulations (Fig. 12). In austral summer (JFM) and winter (JAS) there is
 371 an overwhelming reduction in sea ice thickness surrounding Antarctica. Changes in FWFs around
 372 Antarctica though are masked by the increase in heat loss.

373 Since the MOC was analyzed in σ_2 coordinates, we use the same coordinate for the water mass
 374 analysis. To calculate the time-mean surface water mass transformation, the surface buoyancy flux
 375 (Eq. 11) is integrated over the surface outcrop area as

$$\Omega(\sigma_2) = \frac{1}{g} \frac{\partial}{\partial \sigma_2} \overline{\int_{\mathcal{A}_{\sigma_2}} \mathcal{B} dA} \quad (12)$$

376 where \mathcal{A}_{σ_2} represents integration over the area south of 30° S with density greater than σ_2 . By
 377 breaking \mathcal{B} into Q_o and FWF components, Ω can be decomposed into transformation due to Q_o
 378 (Ω_{HF}) and FWF (Ω_{FWF}). There are additional contributions to water mass transformation due to
 379 interior mixing and cabbeling, but those are not diagnosed here (the necessary model output was
 380 not saved). As shown below, changes in surface transformation can explain most of the changes
 381 in the MOC.

382 Fig. 13 shows the annual mean Ω , Ω_{HF} , and Ω_{FWF} for both control and perturbation experi-
 383 ments. Examining the control case first, we see that Ω contains three peaks, each corresponding
 384 with one of the cells of ψ_{moc} described above and shown in Fig. 8. (The transformation rates
 385 should be compared with the MOC at 30° S.) For the densest waters ($36.6 < \sigma_2 < 37.2 \text{ kg m}^{-3}$)
 386 surface heat fluxes make water denser, with a peak transformation rate of 14 Sv; this corresponds
 387 with the subpolar cell of the MOC. For water of intermediate density ($35.4 < \sigma_2 < 36.6 \text{ kg m}^{-3}$),
 388 a combination of heat and FWFs (the dominant component) makes the water lighter, with a peak
 389 transformation rate of -32 Sv; this corresponds with the upper cell of the MOC. Ω and ψ_{moc} do

390 not match up perfectly, since we have not calculated the transformation due to mixing; however,
391 this component can be inferred as the residual, as shown in Newsom et al. (2015). Mixing causes
392 additional water to be entrained into the subpolar cell; in contrast, mixing weakens the upper cell
393 slightly and redistributes its position in density space.

394 The WP experiment produced a strengthening of both the upper and subpolar MOC cells. Corre-
395 spondingly, in Fig. 13 we see that the transformation rates associated with these cells also increase
396 in magnitude. The increased heat loss associated with the subpolar cell causes transformation to
397 nearly double for water denser than $\sigma_2 = 37.0 \text{ kg m}^{-3}$, to a maximum of 26 Sv, matching the 12
398 Sv increase in overturning almost exactly. Although the upper cell transformation is dominated
399 by FWFs in the control, it is the heat fluxes which change most strongly under the WP; increased
400 density gain due to surface heat flux strengthens the upper-cell transformation to nearly -40 Sv and
401 shifts its maximum from $\sigma_2 = 36.0 \text{ kg m}^{-3}$ to $\sigma_2 = 36.2 \text{ kg m}^{-3}$, again consistent with the 8 Sv
402 increase in the upper cell. Changes in transformation due to FWF changes were minimal, as also
403 found by Newsom et al. (2015) in a greenhouse-warming scenario.

404 The changes in transformation are driven by the changes in heat flux shown in Fig. 11, namely
405 increased heat flux into the ocean in the ACC latitudes and increased heat flux out of the ocean
406 near Antarctica. The physical explanation for this change is likely related to increased Ekman
407 upwelling. In the ACC latitudes, where the water column is stably stratified in temperature, this
408 brings cooler water to the surface and, due to the interactive nature of latent and sensible heat
409 flux, produces increased heat gain. In the subantarctic region, where warmer water lies below
410 the surface, increased upwelling has the opposite effect, producing increased heat loss. Overall,
411 the entire pattern of Southern Ocean circulation and water mass transformation strengthens with
412 increasing winds.

413 **7. Discussion and Conclusions**

414 The Southern Ocean ACC transport and MOC response to changes in wind forcing in a fully-
415 coupled high-resolution climate model (CESM) are diagnosed. Results from a twenty-year wind
416 perturbation experiment, where the Southern Hemisphere winds were increased by 50%, show
417 that the ACC transport is nearly eddy saturated, but the MOC is not eddy compensated. The ACC
418 transport response through Drake Passage only changes marginally. During the first ten years of
419 the simulation, while the eddies are ramping up, the ACC transport has a linear trend of 23 Sv
420 decade⁻¹ in response to the increased wind forcing. After a decade the eddies have reached an
421 equilibrium state and the ACC transport adjusted to the elevated level of EKE. The overall ACC
422 transport only increased by 6% compared to the control simulation suggesting that the ACC is
423 nearly eddy saturated.

424 The MOC does increase in the upper and lower cells by 63% and 39% respectively. Changes
425 in the MOC are connected directly with changes in water mass transformation due to changes
426 in the latitude of potential density surfaces and surface buoyancy forcing. When the MOC is
427 decomposed into mean and transient eddy contributions, the eddy-driven overturning does not
428 change much compared to the control. This result is consistent with the mean upper ocean EKE
429 difference (Fig. 2) where EKE is enhanced and suppressed along the mean path of the ACC. The
430 zonally-integrated mean EKE difference sums to near zero with the areas of eddy suppression,
431 which explains why our transient overturning difference is negligible. EKE is enhanced at choke
432 points along the mean ACC path near major topography and in the Western Boundary Current
433 regions without any systematic shifts in the Southern Ocean SSH fronts.

434 Comparing the MOC results of this study with the same WP experiment (PERT1) performed in
435 the coarse-resolution CCSM4 climate model in GD11, we find a lesser role for transient eddies.

436 The biggest changes in the overturning circulation in our high-resolution experiment arises from
437 enhancement of the steady rather than the transient eddy-induced overturning. When the mean
438 overturning circulation is decomposed into a time and zonal mean and a standing component,
439 the balance of the MOC is approximately between these two components (Eq. 9). As the winds
440 increase, the standing component of the overturning acts to partially, but not perfectly, compensate
441 for the increase in the wind-driven Deacon Cell.

442 In this study we have considered a twenty-year perturbation to the Southern Ocean with eddy-
443 resolving resolution. This simulation pushed the limits of the community's current computational
444 capabilities. Ideally, analyzing the full response of the overturning circulation to a perturbation of
445 this type would require a simulation that is at least an order of magnitude longer. Thus, parame-
446 terization of mesoscale processes is still needed. This simulation, however, does support the study
447 of Thompson and Garabato (2014), which suggests that the equilibration of the ACC to changes
448 in surface wind forcing will principally involve processes that are zonally-asymmetric. A change
449 in the wind stress without an increase in the zonal mean transport requires a greater vertical mo-
450 mentum flux carried out by transient eddies. Thompson and Garabato (2014) argue that changes
451 in eddy activity will be focused in standing meanders related to fluctuations in the amplitude and
452 wavelength of the meander. It is important to note that this response is quite different from the
453 coarse-resolution study of GD11, where the GM coefficient increases almost uniformly through-
454 out the ACC. A key result of this study is that directly resolving mesoscale eddies shows that the
455 response of ACC's EKE, for instance, to changes in wind stress is likely too nuanced to be de-
456 scribed by trends spanning the whole ACC or even basins. We plan to analyze the momentum and
457 vorticity budgets of both high and low resolution simulations, similar to Cronin and Watts (1996)
458 and Hughes (2005) in a future study.

459 There are some potential shortcomings of our simulation. One shortcoming is that the analysis
460 was done using monthly archived data. Ballarotta et al. (2013) found close correspondence in the
461 MOC at 5-day versus monthly archived data, suggesting that most of the signal is at monthly time
462 scales and longer. However, their analysis was done in an eddy-permitting model (0.25°), which
463 does not adequately resolve the first baroclinic deformation radius at these latitudes (Hallberg
464 2013). Encouragingly, Abernathey and Wortham (2015), analyzing the same class of CESM sim-
465 ulation used here, found that mesoscale eddy fluxes were dominated by sub-monthly frequencies.
466 Another shortcoming of this study is the duration of our WP experiment, which was computationally
467 constrained. The model may not have reached an equilibrium state, and obviously not for
468 time scales longer than the twenty year duration of the simulation. Future studies could focus on
469 longer simulations as well as meridional shifts of the mean winds north and south to simulate past
470 climates.

471 With these caveats set aside, the high-resolution simulation has shown how increasing winds
472 could lead to an increase in the MOC on the time scales of twenty years. The results from this
473 study broadly agree with ozone depletion experiments, meant to simulate the increase in zonal
474 wind stress in the Southern Hemisphere during austral summer (Ferreira et al. 2015; Solomon et al.
475 2015). The average SST difference during the last ten years of our WP experiment resemble the
476 the slow time-scale response in Ferreira et al. (2015), in which there is warming around Antarctica
477 and cooling at mid-latitudes (Fig. 4c). The wind stress changes are stronger in our WP experiment
478 than in the ozone depletion studies and as a result we see much more warming, up to 2°C , in
479 places around Antarctica. These results are indicative of an increase in the lower cell of the MOC
480 (Fig. 8), which causes more upwelling of warm and salty Circumpolar Deep Water (CDW). The
481 upwelling of CDW melts more sea ice throughout the year, which leads to an enhancement of
482 FWFs surrounding Antarctica. Increasing winds alone in the Southern Hemisphere may lead to

483 more sea-level rise. The recent trends in winds observed over the past few decades in Southern
484 Hemisphere winds may already be having an influence on the MOC. This would infer that the
485 oceanic uptake of CO₂ may be changing as well.

486 *Acknowledgments.* SPB was supported by the President and Director's Fund at the California
487 Institute of Technology. AFT was supported by NSF grant NSF OCE-1235488. We thank Justin
488 Small for providing the control experiment. Computational resources for the simulation analyzed
489 here was provided by the NCAR Computational and Information Systems Lab under the "Accel-
490 erated Scientific Discovery" program. We also thank Marcus Jochum for helpful comments that
491 improved the manuscript and technical support from Gokhan Danabasoglu. NCAR is supported
492 by the National Science Foundation.

493 References

- 494 Abernathey, R., and P. Cessi, 2014: Topographic enhancement of eddy efficiency in baroclinic
495 equilibration. *Journal of Physical Oceanography*, **44**, 2107–2126.
- 496 Abernathey, R., J. Marshall, and D. Ferreira, 2011: The dependence of Southern Ocean Meridional
497 Overturning on wind stress. *Journal of Physical Oceanography*, **41**, 2261–2278.
- 498 Abernathey, R. P., and C. Wortham, 2015: Phase speed cross spectra of eddy heat fluxes in the
499 pacific. *J. Phys. Oceanogr.*, **45**, 1285–1301, doi:10.1175/JPO-D-14-0160.1.
- 500 Abram, N. J., R. Mulvaney, F. Vimeux, S. J. Phipps, J. Turner, and M. H. England, 2014: Evolution
501 of the Southern Annular Mode during the past millennium. *Nature Climate Change*, **4**, 564–569.
- 502 Ballarotta, M., S. Drijfhout, T. Kuhlbrodt, and K. Döös, 2013: The residual circulation of the
503 Southern Ocean: Which spatio-temporal scales are needed? *Ocean Modelling*, **64**, 46–55.

- 504 Bishop, S. P., and F. O. Bryan, 2013: A comparison of mesoscale eddy heat fluxes from obser-
505 vations and a high-resolution ocean model simulation of the Kuroshio Extension. *Journal of*
506 *Physical Oceanography*, **43**, 2563–2570.
- 507 Böning, C. W., A. Dispert, M. Visbeck, S. R. Rintoul, and F. U. Schwarzkopf, 2008: The response
508 of the Antarctic Circumpolar Current to recent climate change. *Nature Geoscience*, **1**, 864–869.
- 509 Chidichimo, M. P., K. A. Donohue, D. R. Watts, and K. L. Tracey, 2014: Baroclinic transport time
510 series of the Antarctic Circumpolar Current measured in Drake Passage. *Journal of Physical*
511 *Oceanography*, **44**, 1829–1853.
- 512 Cronin, M., and D. R. Watts, 1996: Eddy-mean flow interaction in the Gulf Stream at 68°W. Part
513 I: Eddy energetics. *Journal of Physical Oceanography*, **26** (10), 2107–2131.
- 514 de Szoeke, R. A., and M. D. Levine, 1981: The advective flux of heat by mean geostrophic motions
515 in the Southern Ocean. *Deep Sea Res.*, **28A** (10), 1057–1085.
- 516 Döös, K., and D. J. Webb, 1994: The Deacon cell and the other meridional cells of the Southern
517 Ocean. *Journal of Physical Oceanography*, **24**, 429–442.
- 518 Downes, S. M., and A. M. Hogg, 2013: Southern Ocean circulation and eddy compensation in
519 CMIP5 models. *Journal of Climate*, **26**, 7198–7220.
- 520 Downes, S. M., and Coauthors, 2015: An assessment of southern ocean water masses and sea ice
521 during 1988–2007 in a suite of inter-annual core-ii simulations. *Ocean Modelling*.
- 522 Dufour, C., J. L. Sommer, J. Zika, M. Gehlen, J. Orr, P. Mathiot, and B. Barnier, 2012: Stand-
523 ing and transient eddies in the response of the Southern Ocean Meridional Overturning to the
524 Southern Annular Mode. *Journal of Climate*, **25**, 6958–6974.

- 525 Farneti, R., and Coauthors, 2015: An assessment of Antarctic Circumpolar Current and Southern
526 Ocean Meridional Overturning Circulation sensitivity during 1958–2007 in a suite of interan-
527 nual CORE-II simulations. *Ocean Modelling*, submitted.
- 528 Ferreira, D., J. Marshall, C. M. Bitz, S. Solomon, and A. Plumb, 2015: Antarctic ocean and sea ice
529 response to ozone depletion: A two-time-scale problem. *Journal of Climate*, **28**, 1206–1226.
- 530 Firing, Y. L., T. K. Chereskin, and M. R. Mazloff, 2011: Vertical structure and transport of the
531 Antarctic Circumpolar Current in Drake Passage from direct velocity observations. *Journal of
532 Geophysical Research*, **116 (C08015)**, 16, doi:10.1029/2011JC006999.
- 533 Gent, P., and Coauthors, 2011: The Community Climate System Model version 4. *Journal of
534 Climate*, **24**, 4973–4991.
- 535 Gent, P. R., 2015: Effects of Southern Hemisphere wind changes on the Meridional Overturning
536 Circulation in ocean models. *Annual Review of Marine Science*, in press.
- 537 Gent, P. R., and G. Danabasoglu, 2011: Response to increasing southern hemisphere winds in
538 CCSM4. *Journal of Climate*, **24**, 4992–4998.
- 539 Gent, P. R., and J. C. McWilliams, 1990: Isopycnal mixing in ocean circulating models. *Journal
540 of Physical Oceanography*, **20**, 150–155.
- 541 Gnanadesikan, A., M.-A. Pradal, and R. Abernathey, 2015: Isopycnal mixing by mesoscale ed-
542 dies significantly impacts oceanic anthropogenic carbon uptake. *Geophysical Research Letters*,
543 **42 (11)**, 4249–4255, doi:10.1002/2015GL064100, 2015GL064100.
- 544 Gouretski, V., and K. Koltermann, 2004: WOCE global hydrographic climatology. A technical
545 report. Tech. Rep. 35, Berichte des Bundesamtes für Seeschifffahrt und Hydrographic Nr.

- 546 Hallberg, R., 2013: Using a resolution function to regulate parameterizations of oceanic mesoscale
547 eddies. *Ocean Modelling*, **72**, 92–103.
- 548 Hallberg, R., and A. Gnanadesikan, 2006: The role of eddies in determining the structure and
549 response of wind-driven Southern Hemisphere overturning: Results from the modeling eddies
550 in the Southern Ocean (MESO) project. *Journal of Physical Oceanography*, **36**, 2232–2252.
- 551 Hogg, A. M., M. P. Meredith, D. P. Chambers, E. P. Abrahamsen, C. W. Hughes, and A. K. Mor-
552 rison, 2015: Recent trends in the Southern Ocean eddy field. *Journal of Geophysical Research*,
553 **120**, 257–267, doi:10.1002/2014JC010470.
- 554 Hughes, C., 2005: Nonlinear vorticity balance of the Antarctic Circumpolar Current. *Journal of*
555 *Geophysical Research*, **110**, C11 008, doi:10.1029/2004JC002753.
- 556 Hunke, E., and W. Lipscomb, 2008: CICE: the Los Alamos sea ice model user's manual, version
557 4. Tech. rep., Los Alamos National Laboratory.
- 558 Hurrell, J. W., and Coauthors, 2013: The Community Earth System Model: A framework for
559 collaborative research. *Bulletin of the American Meteorological Society*, **94**, 1339–1360.
- 560 Iudicone, D., G. Madec, and T. J. McDougall, 2008: Water-mass transformations in a neutral
561 density framework and the key role of light penetration. *J. Phys. Oceanogr.*, **38**, 1357–1376.
- 562 Johnson, G. C., and H. L. Bryden, 1989: On the size of the Antarctic Circumpolar Current. *Deep*
563 *Sea Res.*, **36**, 39–53.
- 564 Kirtman, B., and Coauthors, 2012: Impact of ocean model resolution on CCSM climate simula-
565 tions. *Climate Dynamics*, **39**, 1303–1328.
- 566 Large, W. G., and A. J. G. Nurser, 2001: Ocean surface water mass transformation. *Ocean Circu-*
567 *lation and Climate – Observing and Modelling the Global Ocean*, Academic Press.

- 568 Large, W. G., and S. G. Yeager, 2009: The global climatology of an interannually varying air-sea
569 flux data set. *Climate Dynamics*, **33**, 341–364.
- 570 Lawrence, D., and Coauthors, 2011: Parameterization improvements and functional and structural
571 advances in version 4 of the Community Land Model. *Journal of Advances in Modeling Earth
572 Systems*, **3** (2011MS000045).
- 573 Lee, M., and A. Coward, 2003: Eddy mass transport for the Southern Ocean in an eddy-permitting
574 global ocean model. *Ocean Modelling*, **5**, 249–266.
- 575 Lenn, Y.-D., T. K. Chereskin, J. Sprintall, and J. L. McClean, 2011: Near-surface eddy heat and
576 momentum fluxes in the Antarctic Circumpolar Current in Drake Passage. *Journal of Physical
577 Oceanography*, **41**, 1385–1407.
- 578 Marsh, R., A. J. G. Nurser, A. P. Megann, and A. L. New, 2000: Water mass transformation in the
579 Southern Ocean of a global isopycnal coordinate gcm. *J. Phys. Oceanogr.*, **40**, 1013–1045.
- 580 Marshall, J., D. Jamous, and J. Nilsson, 1999: Reconciling thermodynamic and dynamic methods
581 of computation of water-mass transformation rates. *Deep Sea Res. I*, **46**, 545–572.
- 582 Marshall, J., D. Olbers, H. Ross, and D. Wolf-Gladrow, 1993: Potential vorticity constraints on
583 the dynamics and hydrography of the Southern Ocean. *J. Phys. Oceanogr.*, **23**, 465–487.
- 584 Marshall, J., and T. Radko, 2003: Residual-mean solutions for the Antarctic Circumpolar Current
585 and its associated Overturning Circulation. *Journal of Physical Oceanography*, **33**, 2341–2354.
- 586 Marshall, J., and K. Speer, 2012: Closure of the meridional overturning circulation through South-
587 ern Ocean upwelling. *Nature Geoscience*, **5**, 171–180.
- 588 McClean, J., and Coauthors, 2011: A prototype two-decade fully-coupled fine-resolution CCSM
589 simulation. *Ocean Modelling*, doi:doi:10.1016/j.ocemod.2011.02.011.

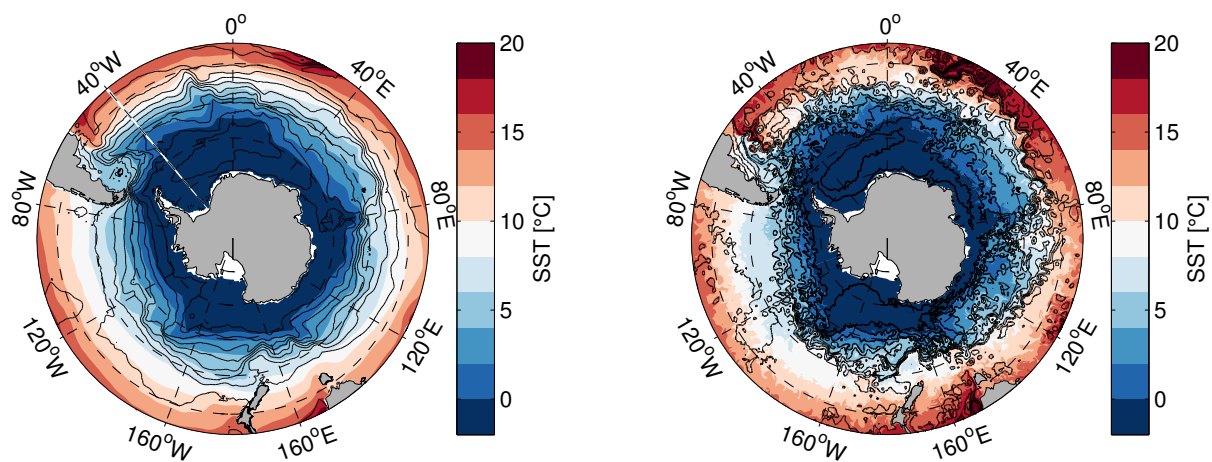
- 590 Meredith, M. P., and A. M. Hogg, 2006: Circumpolar response of Southern Ocean eddy activity
591 to a change in the Southern Annular Mode. *Geophysical Research Letters*, **33**, L16608, doi:
592 10.1029/2006GL026499.
- 593 Morrison, A. K., T. L. Frölicher, and J. L. Sarmiento, 2015: Upwelling in the Southern Ocean.
594 *Physics Today*, **68**, 27–32.
- 595 Morrison, A. K., and A. M. Hogg, 2013: On the relationship between Southern Ocean Overturning
596 and ACC transport. *Journal of Physical Oceanography*, **43**, 140–148.
- 597 Munday, D. R., H. L. Johnson, and D. P. Marshall, 2013: Eddy saturation of equilibrated circum-
598 polar currents. *Journal of Physical Oceanography*, **43**, 507–532.
- 599 Newsom, E., C. Bitz, F. Bryan, R. P. Abernathey, and P. Gent, 2015: Sea ice processes control
600 abyssal Southern Ocean heat uptake in a fine resolution ocean climate model, manuscript sub-
601 mitted to *J. Phys. Oceanogr.*
- 602 Nikurashin, M., and G. Vallis, 2012: A theory of the interhemispheric meridional overturning
603 circulation and associated stratification. *J. Phys. Oceanogr.*, **42**, 1652–1667.
- 604 Sallée, J.-B., R. J. Matear, S. R. Rintoul, and A. Lenton, 2012: Localized subduction of anthro-
605 pogenic carbon dioxide in the Southern Hemisphere oceans. *Nature Geoscience*, **5**, 579–584.
- 606 Small, R. J., and Coauthors, 2014: A new high-resolution global climate simulation using Comm-
607 nunity Atmosphere Model version 5. *Journal of Advances in Modeling Earth Systems*, **6**, 1065–
608 1094, doi:10.1002/2014MS000363.
- 609 Smith, K. S., 2007: The geography of linear baroclinic instability in Earth's oceans. *Journal of*
610 *Marine Research*, **65**, 655–683.

- 611 Solomon, A., L. Polvani, K. Smith, and R. Abernathey, 2015: The impact of ozone depleting
612 substances on the circulation, temperature, and salinity of the Southern Ocean: An attribution
613 study with CESM1 (WACCM). *Geophysical Research Letters*, **42**, 5547–5555, doi:10.1002/
614 2015GL064744.
- 615 Speer, K., and E. Tziperman, 1992: Rates of water mass formation in the North Atlantic Ocean. *J.
616 Phys. Oceanogr.*, **22**, 93–104.
- 617 Stewart, A. L., R. Ferrari, and A. F. Thompson, 2014: On the importance of surface forcing in
618 conceptual models of the deep ocean. *Journal of Physical Oceanography*, **44**, 891–899.
- 619 Straub, D., 1993: On the transport and angular momentum balance of channel models of the
620 Antarctic Circumpolar Current. *Journal of Physical Oceanography*, **23**, 776–782.
- 621 Thompson, A. F., and A. C. N. Garabato, 2014: Equilibration of the Antarctic Circumpolar Current
622 by standing meanders. *Journal of Physical Oceanography*, **44**, 1811–1828.
- 623 Thompson, D. W., S. Solomon, P. J. Kushner, M. H. England, K. M. Grise, and D. J. Karoly, 2011:
624 Signatures of the Antarctic ozone hole in Southern Hemisphere surface climate change. *Nature
625 Geoscience*, doi:DOI:10.1038/NGEO1296.
- 626 Toggweiler, J. R., 2009: Shifting Westerlies. *Science*, **323**, 1434–1435.
- 627 Treguier, A. M., and J. C. McWilliams, 1990: Topographic influences on wind-driven, stratified
628 flow in a beta-plane channel: An idealized model for the antarctic circumpolar current. *J. Phys.
629 Oceanogr.*, **20 (3)**, 321–343.
- 630 Tziperman, E., 1986: On the role of interior mixing and air-sea fluxes in determining the stratifi-
631 cation and circulation of the oceans. *J. Phys. Oceanogr.*, **16**, 680–693.

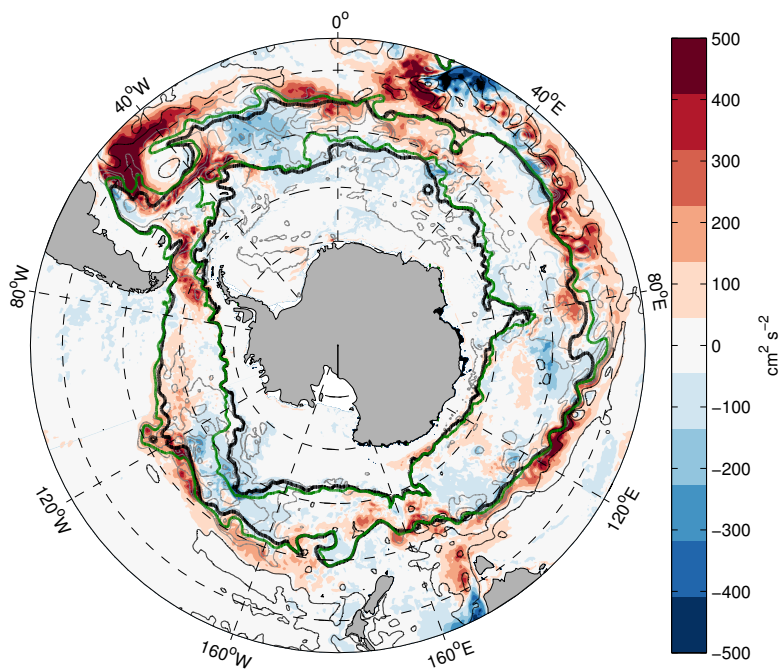
- 632 Viebahn, J., and C. Eden, 2012: Standing eddies in the Meridional Overturning Circulation. *Journal*
633 *of Physical Oceanography*, **42**, 1486–1508.
- 634 Volkov, D. L., L.-L. Fu, and T. Lee, 2010: Mechanisms of the meridional heat transport in the
635 Southern Ocean. *Ocean Dynamics*, **60**, 791–801.
- 636 Walin, G., 1982: On the relation between sea-surface heat flow and thermal circulation in the
637 ocean. *Tellus*, **34**, 187–195.
- 638 Wolfe, C. L., and P. Cessi, 2010: What sets the strength of the middepth stratification and overturn-
639 ing circulation in eddyng ocean models? *Journal of Physical Oceanography*, **40**, 1520–1538.
- 640 Wolff, J.-O., E. Maier-Reimer, and D. J. Olbers, 1991: Wind-driven flow over topography in a
641 zonal beta-plane channel: A quasi-geostrophic model of the Antarctic Circumpolar Current. *J.
642 Phys. Oceanogr.*, **21**, 263–291.
- 643 Zika, J. D., and Coauthors, 2013: Vertical eddy fluxes in the Southern Ocean. *Journal of Physical
644 Oceanography*, **43**, 941–955.

645 LIST OF FIGURES

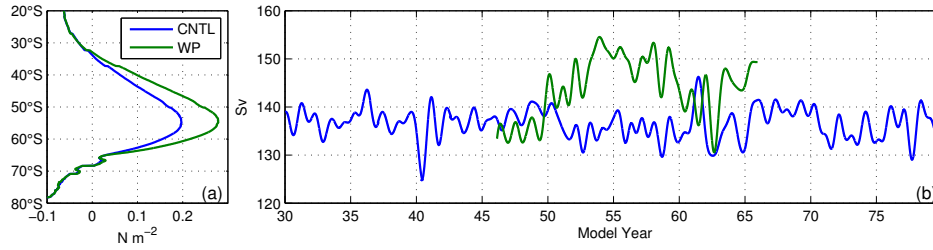
646	Fig. 1. Snap shots of austral winter SST and SSH in low- (left) and high-resolution (right) CESM.	32
647	Color contours are SST ($ci = 1^{\circ}\text{C}$) and black contours are SSH ($ci = 25 \text{ cm}$).	
648	Fig. 2. Change in EKE (WP-CNTL) for model years 56–65. Change in EKE for the upper 1000 m	33
649	(color contours, $ci = 50 \text{ cm}^2 \text{ s}^{-2}$) with black (positive) and gray (negative) contours ($ci =$	
650	10 cm) the change in mean SSH. The thick black (CNTL) and green (WP) contours are the	
651	-150 and -25 cm mean SSH contours that pass through Drake Passage.	
652	Fig. 3. (a) Time and zonal mean zonal wind stress for the control and WP experiments for model	34
653	year 56–65. (b) One-year low-pass filtered times series of Drake Passage transport using a	
654	fourth-order Butterworth filter centered around model years 45–66. The first and last year	
655	of each time series was removed due to Gibbs ringing at the end points.	
656	Fig. 4. Sea surface density, temperature, and salinity differences between the control and WP ex-	35
657	periments for model years 56–65. (a) Density difference (color contours, $ci = 0.05 \text{ kg m}^{-3}$).	
658	(b) Zonal average surface density. (c) SST color contours ($ci = 0.25^{\circ}\text{C}$). (d) Zonal average	
659	SST. (e) Salinity differences ($ci = 0.1 \text{ g kg}^{-1}$). (f) Zonal average salinity. Black (control)	
660	and gray (WP) contours in (a), (c), and (e) are mean density contours ($ci = 0.25 \text{ kg m}^{-3}$).	
661	Fig. 5. (a) Area-average time series of daily surface EKE anomaly referenced to the control mean	36
662	derived from daily SSH. (b) 10-year linear trend in EKE for model years 45–56 in the WP	
663	experiment (color contours, $ci = 50 \text{ cm}^2 \text{ s}^{-2} \text{ decade}^{-1}$). Light gray contours are mean SSH	
664	($ci = 25 \text{ cm}$).	
665	Fig. 6. Differences between the time and zonal mean σ_2 (WP-CNTL) for model years 56–65. (a)	37
666	Full water column. Color contours are the differences with $ci = 0.01 \text{ kg m}^{-3}$. (b) Same as in	
667	(a), but for the upper ocean. The black and gray contours in both are the depth of the time	
668	and zonal mean σ_2 surfaces in the control and WP simulations respectively with $ci = 0.25$	
669	kg m^{-3} . (c) Probability density distribution for potential density differences.	
670	Fig. 7. The Eulerian-mean MOC (Eq. 1) for the control (a), WP (b), and difference (c). The color	38
671	contours are the overturning streamfunction in units of Sv with $ci = 2 \text{ Sv}$ for (a) and (b) and	
672	$ci = 1 \text{ Sv}$ for (c). The black and gray contours are the depth of the time and zonal mean σ_2	
673	surfaces in the control and WP simulations respectively with $ci = 0.25 \text{ kg m}^{-3}$	
674	Fig. 8. MOC (ψ_{moc} , a–c), mean overturning circulation ($\bar{\psi}$, d–f), and transient eddy overturning	39
675	circulation (ψ^* , g–i) for the control (left column), WP (middle column), and difference	
676	(right column, WP minus control). Color contours have $ci = 1 \text{ Sv}$. Black and gray contours	
677	are positive and negative overturning circulation respectively with $ci = 5 \text{ Sv}$	
678	Fig. 9. Mean overturning circulation, $\bar{\psi}$, decomposed into the time and zonal mean, $[\bar{\psi}]$, and stand-	40
679	ing, ψ^\dagger , overturning circulation. Mean overturning (a–c, same as d–f in Fig. 8), time and	
680	zonal mean overturning (d–f), and standing overturning circulation (g–i) for the control (left	
681	column), WP (middle column), and difference (right column, WP minus control). Color	
682	contours have $ci = 1 \text{ Sv}$. Black and gray contours are positive and negative overturning	
683	circulation respectively with $ci = 5 \text{ Sv}$	
684	Fig. 10. The change in the time and zonal mean kinetic energy (Eq. 10) between the WP and control	41
685	simulations for model years 56–65.	



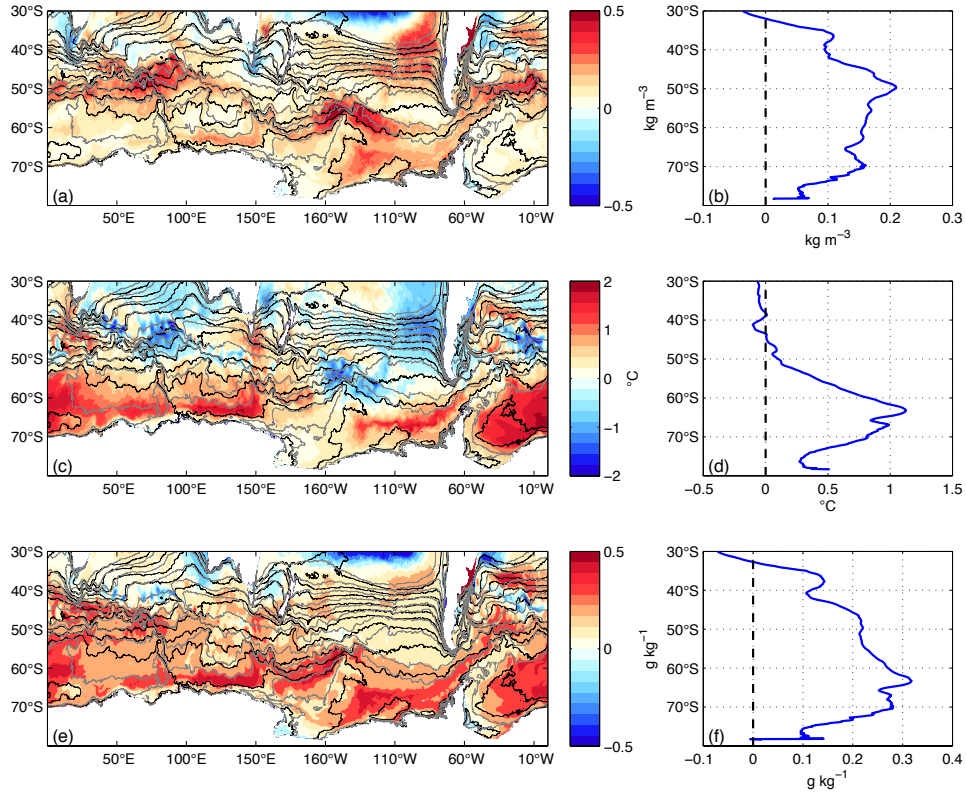
698 FIG. 1. Snap shots of austral winter SST and SSH in low- (left) and high-resolution (right) CESM. Color
699 contours are SST ($\text{ci} = 1^\circ\text{C}$) and black contours are SSH ($\text{ci} = 25 \text{ cm}$).



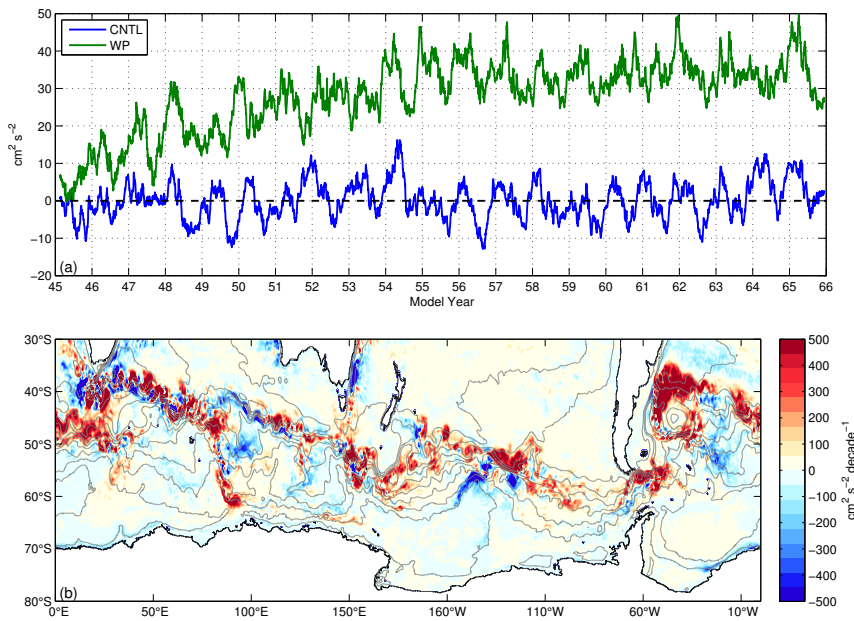
700 FIG. 2. Change in EKE (WP-CNTL) for model years 56–65. Change in EKE for the upper 1000 m (color
 701 contours, $\text{ci} = 50 \text{ cm}^2 \text{s}^{-2}$) with black (positive) and gray (negative) contours ($\text{ci} = 10 \text{ cm}$) the change in mean
 702 SSH. The thick black (CNTL) and green (WP) contours are the -150 and -25 cm mean SSH contours that pass
 703 through Drake Passage.



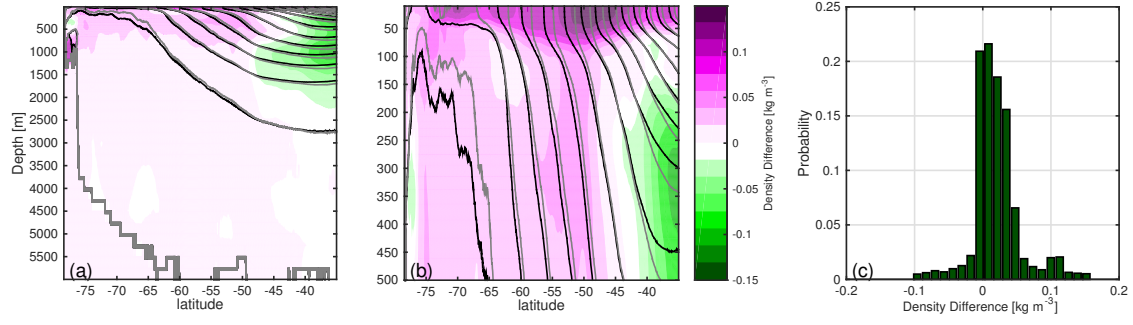
704 FIG. 3. (a) Time and zonal mean zonal wind stress for the control and WP experiments for model year 56–
 705 65. (b) One-year low-pass filtered times series of Drake Passage transport using a fourth-order Butterworth filter
 706 centered around model years 45–66. The first and last year of each time series was removed due to Gibbs ringing
 707 at the end points.



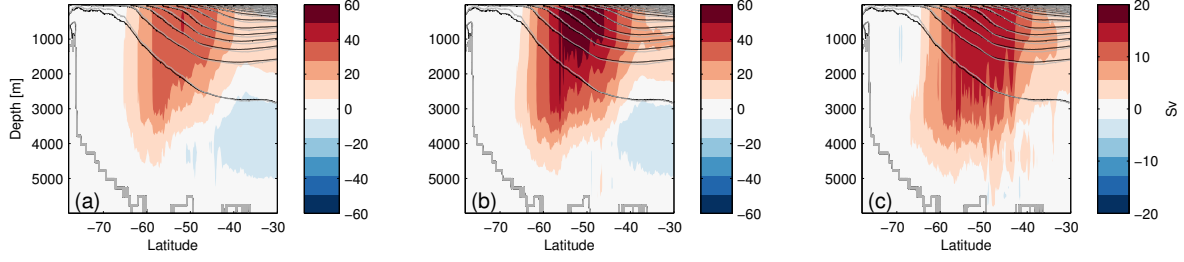
708 FIG. 4. Sea surface density, temperature, and salinity differences between the control and WP experiments
 709 for model years 56–65. (a) Density difference (color contours, $ci = 0.05 \text{ kg m}^{-3}$). (b) Zonal average surface
 710 density. (c) SST color contours ($ci = 0.25 \text{ }^{\circ}\text{C}$). (d) Zonal average SST. (e) Salinity differences ($ci = 0.1 \text{ g kg}^{-1}$).
 711 (f) Zonal average salinity. Black (control) and gray (WP) contours in (a), (c), and (e) are mean density contours
 712 ($ci = 0.25 \text{ kg m}^{-3}$).



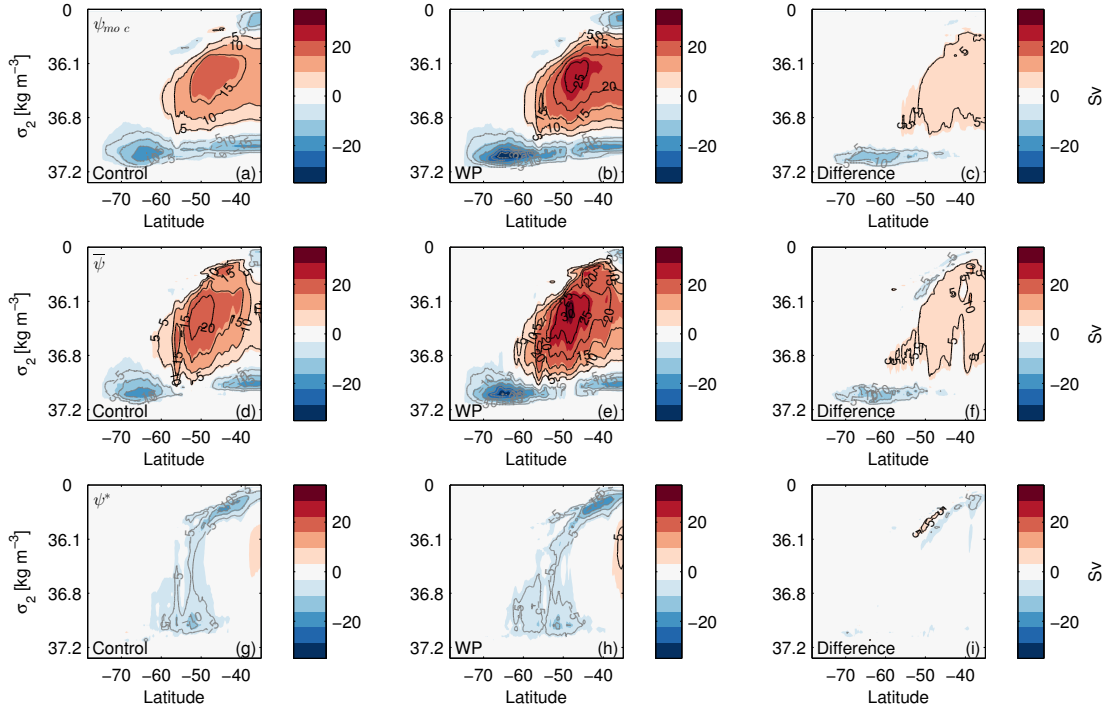
713 FIG. 5. (a) Area-average time series of daily surface EKE anomaly referenced to the control mean derived
 714 from daily SSH. (b) 10-year linear trend in EKE for model years 45–56 in the WP experiment (color contours,
 715 $\text{ci} = 50 \text{ cm}^2 \text{s}^{-2} \text{decade}^{-1}$). Light gray contours are mean SSH ($\text{ci} = 25 \text{ cm}$).



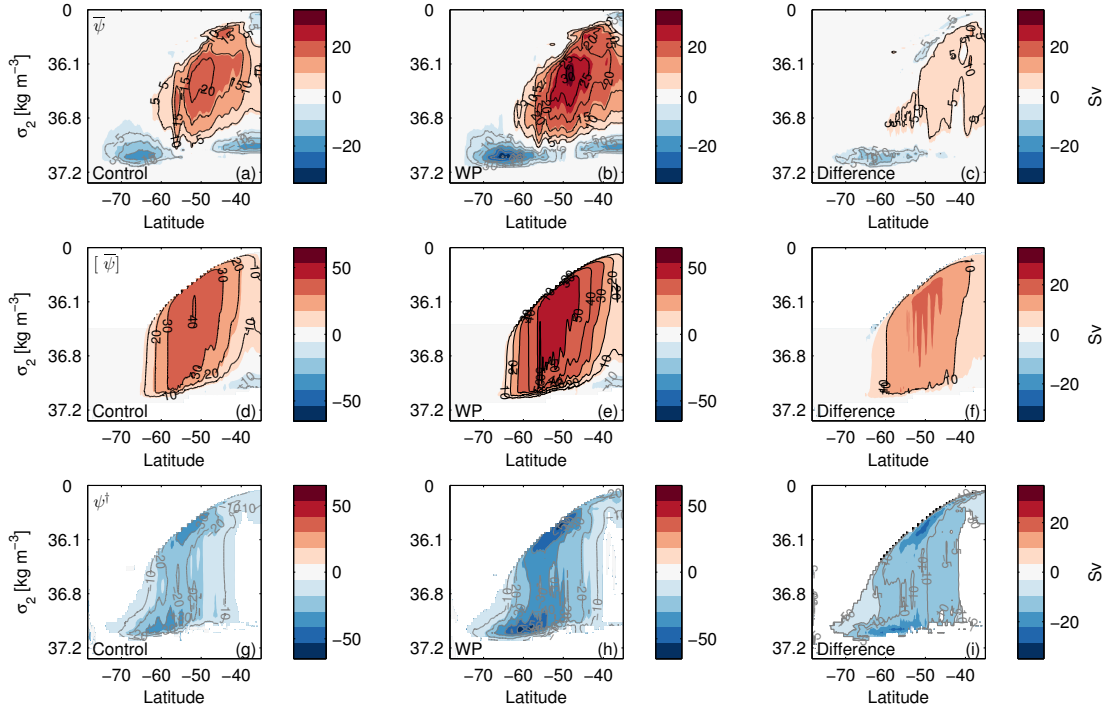
716 FIG. 6. Differences between the time and zonal mean σ_2 (WP-CNTL) for model years 56–65. (a) Full water
 717 column. Color contours are the differences with $c_i = 0.01 \text{ kg m}^{-3}$. (b) Same as in (a), but for the upper ocean.
 718 The black and gray contours in both are the depth of the time and zonal mean σ_2 surfaces in the control and
 719 WP simulations respectively with $c_i = 0.25 \text{ kg m}^{-3}$. (c) Probability density distribution for potential density
 720 differences.



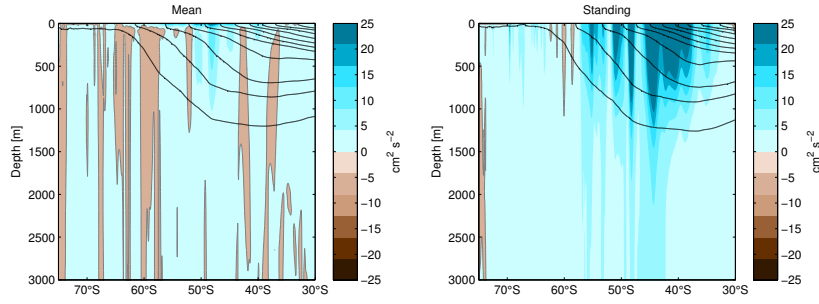
721 FIG. 7. The Eulerian-mean MOC (Eq. 1) for the control (a), WP (b), and difference (c). The color contours
 722 are the overturning streamfunction in units of Sv with $c_i = 2 \text{ Sv}$ for (a) and (b) and $c_i = 1 \text{ Sv}$ for (c). The
 723 black and gray contours are the depth of the time and zonal mean σ_2 surfaces in the control and WP simulations
 724 respectively with $c_i = 0.25 \text{ kg m}^{-3}$.



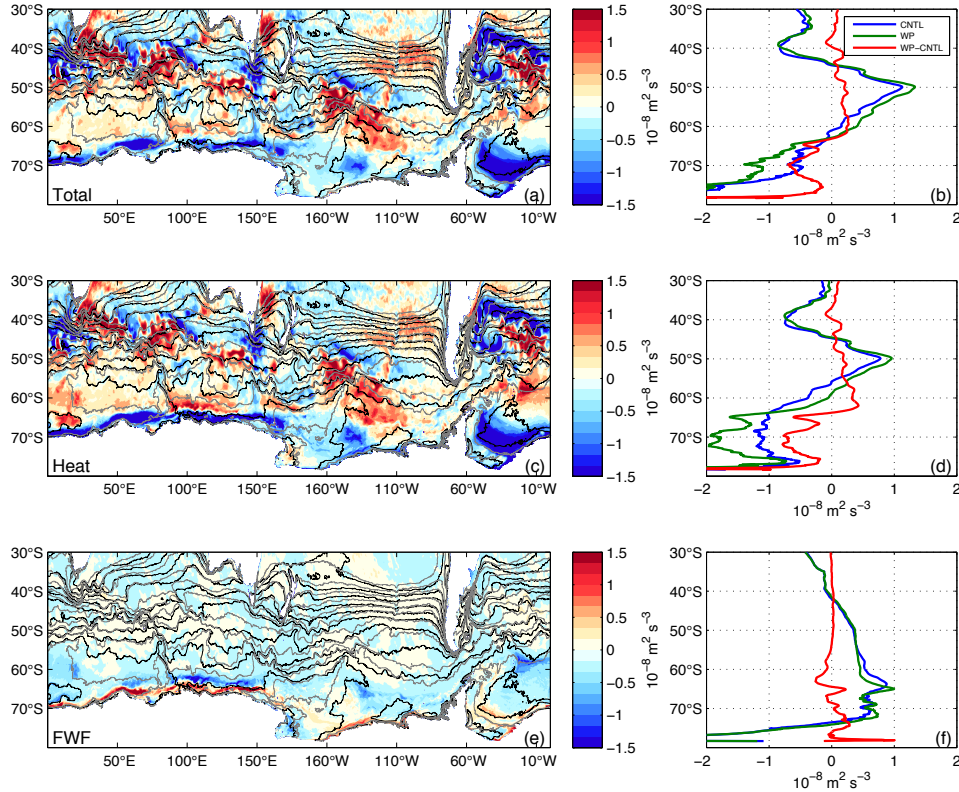
725 FIG. 8. MOC (ψ_{moc} , a–c), mean overturning circulation ($\bar{\psi}$, d–f), and transient eddy overturning circulation
 726 (g–i) for the control (left column), WP (middle column), and difference (right column, WP minus con-
 727 trol). Color contours have $c_i = 1 \text{ Sv}$. Black and gray contours are positive and negative overturning circulation
 728 respectively with $c_i = 5 \text{ Sv}$.



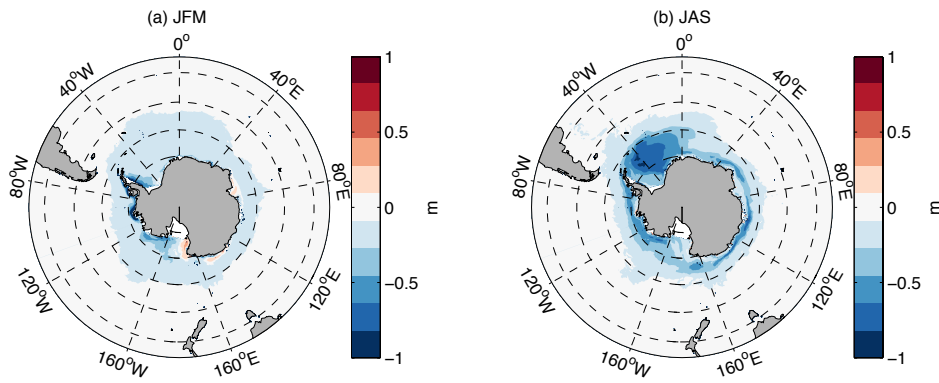
729 FIG. 9. Mean overturning circulation, $\bar{\psi}$, decomposed into the time and zonal mean, $[\bar{\psi}]$, and standing, ψ^\dagger ,
 730 overturning circulation. Mean overturning (a–c, same as d–f in Fig. 8), time and zonal mean overturning (d–f),
 731 and standing overturning circulation (g–i) for the control (left column), WP (middle column), and difference
 732 (right column, WP minus control). Color contours have $ci = 1 \text{ Sv}$. Black and gray contours are positive and
 733 negative overturning circulation respectively with $ci = 5 \text{ Sv}$.



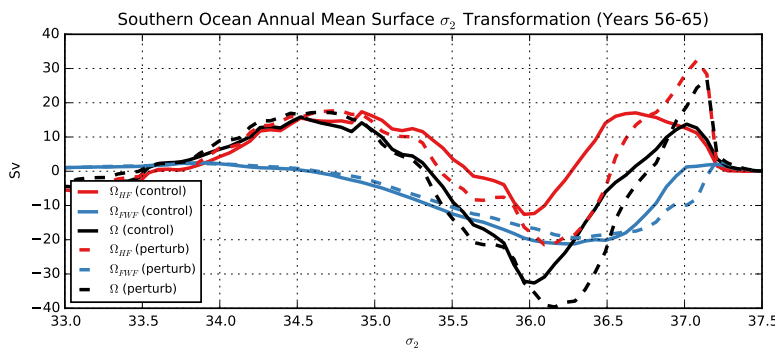
734 FIG. 10. The change in the time and zonal mean kinetic energy (Eq. 10) between the WP and control
 735 simulations for model years 56–65.



736 FIG. 11. Surface buoyancy flux differences between the control and WP experiments for model years 56–65.
 737 (a) is total surface buoyancy and (c) and (e) are contributions from heat and fresh water fluxes respectively (ci
 738 = $0.25 \times 10^{-8} \text{ m}^2 \text{s}^{-3}$). (b), (d), and (f) are zonal average total surface buoyancy, heat, and fresh water flux
 739 contributions. Black (control) and gray (WP) contours in (a), (c), and (e) are mean density contours (ci = 0.25
 740 kg m^{-3}).



741 FIG. 12. Sea ice thickness difference between the control and WP experiments for model years 56–65. (a)
 742 JFM (January, February, March) and (b) JAS (July, August, September) difference ($ci = 0.1$ m).



743 FIG. 13. Surface water mass transformation in control (solid) and perturbation (dashed) experiments. The
 744 heat-flux-driven transformation is in red, the freshwater-flux-driven transformation is in blue, and the net trans-
 745 formation is in black. Positive values mean indicate water being made denser.